Central cell corrections to shallow acceptor states in silicon including noncubic terms

Jianhua Zhu [1,2,3,*] Ji Chen,[2,4,5,†] and Andrew J. Fisher [3,‡]

[1]*School of Mathematics And Physics, University of Science and Technology Beijing, Xueyuan Road 30, Haidian, Beijing 100083, China*
[2]*School of Physics, Peking University, Chengfu Road 209, Haidian, Beijing 100871, China*
[3]*UCL Department of Physics and Astronomy and London Centre for Nanotechnology, University College London,*
Gower Street, London WC1E 6BT, United Kingdom
[4]*Interdisciplinary Institute of Light-Element Quantum Materials and Research Center for Light-Element Advanced Materials,*
Peking University, Beijing 100871, China
[5]*Frontiers Science Center for Nano-Optoelectronics, Peking University, Beijing 100871, China*

The diffuse states in acceptor systems mean they are still largely inaccessible to fully *ab initio* treatments, so the field largely relies on effective-mass theory. However, it has not been clear whether local departures from the cubic symmetry of the bulk semiconductors are important. Here, we present a detailed first-principles study of the central cell corrections for Group III acceptors (B, Al, Ga, and In) in silicon and in particular analyze the noncubic contributions. We simulate an array of nearly isolated acceptors within density functional theory (DFT) and study the resulting band structure of the doped systems. Based on the self-consistent one-electron potentials, we compute central cell corrections for a distorted lattice, where both structures are separately relaxed to the minimum-energy configuration. We find that, although noncubic corrections are substantial close to the acceptor, their influence on the long-range structure of the bound states is minimal because the corrections are localized in a very small range, in contrast with the case of donors in silicon. The corrected states are more localized than the uncorrected ones, so previous estimates of the inter-acceptor distances at which different interactions dominate need to be reduced; our corrections lead to improved agreement with experiment and also allow the different characteristics of different Group III acceptors to be accounted for.

I. INTRODUCTION

Recently, defects in semiconductors have attracted increasing interest because of their potential applications in quantum simulation and quantum computation [1]. Silicon, one of the most widely used materials in the semiconductor industry, is a particularly popular candidate as a host because of the exceptional levels of purity attainable and the low density of nuclear spins. Donors were originally proposed as the qubit-bearing defects [2]; they can be implanted in predetermined locations [3] and have the advantage of very weak spin-orbit coupling and long relaxation and coherence times [4,5]; single-qubit [6] and two-qubit operations [7] and quantum simulation of simple one-dimensional topological models [8] have all been demonstrated using this platform. However, acceptors have also attracted attention recently because the strong spin-orbit coupling in the valence band makes possible

electrically driven operations on the spin [9,10] and quantum simulation of strongly interacting quantum lattice models with nontrivial topological structure. Recently, $AlCl_3$ and BCl_3 were investigated as possible molecular precursors for the incorporation of acceptors on Si(100) to produce atomically precise acceptor-based devices [11,12].

The main features of both donor and acceptor impurities can be understood from a hydrogenic model where a band electron (or hole) feels a long-range Coulomb attraction from a positive donor core (or a negative acceptor core). This approach makes all acceptors (and all donors) equivalent to one another in a given semiconductor host. Recent work on the properties of multi-acceptor structures, including studies of the exchange and quadrupolar interactions between acceptor pairs [13,14] and of the formation of topological states in more complex acceptor arrays [15–17], has been entirely based on the generic Coulomb model.

However, it has long been understood that there are in fact significant quantitative differences between different donors and acceptors; corrections to the Coulomb model are therefore needed (especially at small distances) [18] in order to describe them. In particular, the tetrahedral arrangement of the nearest silicon neighbors around a substitutional impurity (as shown in Fig. 1), which lowers the local symmetry from O_h in the bulk band-structure to T_d, indicates that a symmetry-breaking correction is in principle required. For a single donor, it has been shown that a noncubic central cell correction shows rich

---

*Contact author: ucapjhz@ucl.ac.uk
†Contact author: ji.chen@pku.edu.cn
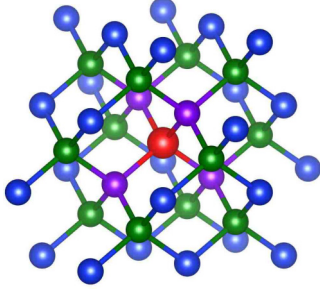‡Contact author: andrew.fisher@ucl.ac.uk

FIG. 1. The structure of doped silicon: the red ball stands for the dopant, while other balls are silicon atoms (purple balls are the nearest neighbors, and green balls are the next-nearest neighbors).

additional physics [19]. However, until now there has been no similar investigation into acceptors.

As shown by Refs. [20–22], the Hamiltonian for holes can be written within the envelope-function approximation and in scaled atomic units (energies measured in units of the effective Rydberg $R_0 = 24.8$ meV, lengths in effective Bohr radii $a_0 = 2.55$ nm) in terms of second-rank tensors $I^{(2)}$ and $P^{(2)}$ constructed from the intrinsic orbital angular momentum operator $\vec{I}$ and the momentum $\vec{p}$, respectively,

$$\hat{H}_c = \frac{p^2}{\hbar^2} + V_{\text{eff}}(\vec{r}) - \frac{\mu}{3\hbar^2}(P^{(2)} \bullet I^{(2)}) + \frac{2}{3}\Delta\left(\frac{1}{2} - \vec{I} \bullet \vec{S}\right)$$
$$+ \frac{\delta}{3\hbar^2}\left([P^{(2)} \times I^{(2)}]_4^{(4)} + \frac{\sqrt{70}}{5}[P^{(2)} \times I^{(2)}]_0^{(4)}\right.$$
$$\left. + [P^{(2)} \times I^{(2)}]_{-4}^{(4)}\right), \quad (1)$$

where p is the hole linear momentum operator, μ is the strength of the spherically symmetric heavy-hole light-hole coupling, Δ is the spin-orbit coupling, and δ is the strength of the cubic anisotropy term [20–22]. In the case of an ideal effective mass impurity, V_{eff} is simply the Coulomb interaction

$$V_{\text{eff}}(\vec{r}) = -\frac{2}{|\vec{r}|}. \quad (2)$$

However, the model has significant limitations. As potential (2) is only valid in the long-range limit, calculations involving small separations are not accurate and this may influence the robustness of previous conclusions. Furthermore, as all parameters in Eq. (1) are determined only by the host semiconductor, the influence from the elemental type of the acceptor is not captured at all in this model. This means the model cannot be meaningfully applied to systems with multiple types of acceptors, or to studying trends between different elements.

Our strategy in this paper is to estimate the non-Coulomb corrections to V_{eff} by high-quality electronic structure calculations close to the defect core and then evaluate the effect of deviations from pure Coulomb behavior on the long-range structure of the shallow hole states using Eq. (1).

In the next section, we give a brief introduction to the methods used, including the setting for the first-principles density functional theory (DFT) calculations. Then we derive central cell corrections for acceptors in silicon by analyzing

TABLE I. The cell sizes and k-point meshes used in the DFT calculations, together with the corresponding densities of acceptors in the supercell array.

Number of atoms	Cell size (Å)	Mesh	Density of acceptors (m^{-3})
8	5.466	$12 \times 12 \times 12$	6.12×10^{27}
64	10.93	$6 \times 6 \times 6$	7.65×10^{26}
216	16.40	$4 \times 4 \times 4$	2.27×10^{26}
512	21.87	$3 \times 3 \times 3$	9.57×10^{25}

short-range deviations from the Coulomb model in DFT. We then explore the consequences of the corrected Hamiltonian for the properties of multi-acceptor structures, using the topological insulator phase recently predicted for a honeycomb-like array of implanted acceptors in silicon [17] as an example. At the end of the paper, we discuss the implications of our corrected model for future research and draw some general conclusions.

II. METHODS

A. First-principles density functional theory (DFT) calculations

First-principles density functional theory (DFT) calculations are used to achieve accurate descriptions of the band structure and local potential for supercells corresponding to both pure and doped silicon systems; in the doped case we introduce one acceptor per unit cell. The projector augmented wave (PAW) method is used as implemented in the VASP package [23,24] and spin-orbit coupling is included. The Perdew-Burke-Ernzerhof (PBE) exchange-correlation function is used in all the calculations. All supercells are simple cubic, based on multiples of the eight-atom conventional cubic cell; the k-point meshes are adjusted as the cell size changes to achieve a constant sampling density in reciprocal space equivalent to 6912 k-points in the Brillouin zone of pure silicon. As we show in Sec. III within the Supplemental Material (SM) [25], the atomic geometry near the defect is well converged at our largest two cell sizes. Details of the k-point meshes and the relevant cells are shown in Table I. The geometry relaxations are performed in the presence of spin-orbit coupling. We use a Gaussian smearing parameter $\sigma = 0.02$ eV for the electron occupation numbers. The internal atomic positions are relaxed until all the forces are smaller than 0.001 eV/Å; the overall supercell dimensions are fixed, corresponding to constant-volume relaxation. We use a cubic lattice constant $a = 5.466$ Å, which we obtained by relaxing the equilibrium volume of pure silicon within DFT using the same projectors and plane-wave cutoff. These values are used for all the calculations in this work. We use a plane-wave cutoff of 350 eV for the case of a B impurity and 300 eV for the other dopants; the default VASP PAW projectors for all elements are used.

B. Symmetries and nature of the acceptor states

When $\delta = 0$, the Hamiltonian (1) has spherical symmetry [20] and the total angular momentum $\vec{F} = \vec{L} + \vec{I} + \vec{S} = \vec{L} + \vec{J}$ is a constant of the motion. Here, $\vec{L}$ is the orbital

angular momentum of the envelope function and $\vec{J} = \vec{I} + \vec{S}$ is the intrinsic angular momentum of a valence-band electron, containing both orbital ($\vec{I}$) and spin ($\vec{S}$) components. There is a corresponding magnetic quantum number m_F for the total angular momentum projection in the z direction. The acceptor eigenstates in the spherical approximation can then be expanded as linear combinations of a group of states with spherical symmetry labeled by the same quantum numbers $\{L, J, F, m_F\}$.

The cubic terms in Hamiltonian (1) couple states with $\Delta m_F = 0, \pm 4$; in the presence of these terms, the eigenstates are instead labeled by irreducible representations of the cubic double group (O_h group). There are six fermionic representations, $\Gamma_6^{\pm}$, $\Gamma_7^{\pm}$, $\Gamma_8^{\pm}$. These states can be obtained by taking suitable linear combinations of states with spherical symmetry. We will only consider the components in Γ^+ states up to a maximum total angular momentum $F = \frac{7}{2}$ and the components in Γ^- states up to $F = \frac{9}{2}$, so the general forms of states from row α of the irreducible representations Γ_8^+ and Γ_8^- states are

$$\Phi(\Gamma_8^+, \alpha) = \sum_{i=1}^{9} f_i(r)|L_i, J_i, F_i, \alpha\rangle, \tag{3}$$

$$\Phi(\Gamma_8^-, \alpha) = \sum_{i=1}^{15} f_i(r)|L_i, J_i, F_i, \alpha\rangle. \tag{4}$$

Here $f_i(r)$ are independent radial parts that can be expanded in terms of Gaussian functions (as described in Sec. II C), and $|L, J, F, \alpha\rangle$ is a symmetry-adapted angular function consisting of appropriate linear combinations of the states $|L, J, F, m_F\rangle$ in the form

$$|L, J, F, \alpha\rangle = \sum_{m_F} M_{\alpha, m_F} |L, J, F, m_F\rangle \tag{5}$$

where the elements of the transformation matrix elements **M** can be found by the method described in Sec. I within the SM [25]. State labels $\{L, J, F\}$ are listed in Table S1 within the SM [25].

The local symmetry around the substitutional impurity is tetrahedral, rather than cubic, and the overall symmetry is therefore T_d. Since this group does not contain the inversion operation, the representations $\Gamma_8^{\pm}$ lose their separate identities (similarly for $\Gamma_6^{\pm}$ and $\Gamma_7^{\pm}$); the central cell correction will therefore contain terms of T_d symmetry, which will couple the Γ_8^+ and Γ_8^- states given above. The result is a Γ_8 ground state, which in general contains all the components in Eqs. (3) and (4).

C. Gaussian basis expansion

The single-acceptor problem Eq. (1) can be solved by expanding the radial part of the envelope function of the eigenstates in terms of Gaussian functions. The radial parts of the states are given by

$$f_i(r) = r^l \sum_j A_j e^{-\alpha_j r^2}, \tag{6}$$

where l is the orbital angular momentum of the envelope function and α_j is a Gaussian exponent. In this paper, we take a set of five Gaussian exponents scaled in a geometrical sequence, with $\alpha_j = \frac{\alpha_0}{r^{j-1}}$ with largest exponent $\alpha_0 = 100\, a_0^{-2}$ and ratio $r = 4.0$. This basis is shown to be an adequate approximation in Sec. II within the SM [25].

D. The alignment of the acceptor potential and binding energy

Our approach is to evaluate the difference between the self-consistent Kohn-Sham potentials with and without the acceptor, then fit this to the screened Coulomb potential (7) plus a short-range "central cell" correction. We then approximate the potential for an electron at an isolated acceptor by the *unscreened* Coulomb potential plus the same central cell correction; this is justified because, as we show below, the central cell correction acts over a distance much smaller than the screening length. We introduce experimental information on the binding energy of the acceptors [26] into our fitting step to get a more accurate ground-state energy, and also to take account of the fact that the local potential computed in DFT has to be supplemented by the action of the PAW projectors within the acceptor core $r \leqslant R_{\mathrm{MAX}}$ (the largest distance that the PAW projectors will influence).

This difference of local potentials would be constrained to have an average of zero over the unit cell if only the electrostatic terms were included, because the $G = 0$ component is excluded from the solution of the Poisson equation in the plane-wave approach. In practice, however, there is a small difference in the average values arising from the inclusion of the exchange-correlation potential. We therefore shift the two potentials such that they share the same value at the furthest position away from the acceptor in the supercell; this position is located along the $\langle 111 \rangle$ direction, at the grid point closest to the body-centered position within the simple cubic supercell. The corresponding shifts (which always increase the self-consistent potential experienced by the electrons) are: for B, 56.68 meV; for Al, 48.18 meV; for Ga, 64.33 meV; for In, 40.02 meV. These shifts are also applied when estimating the binding energy of the acceptors from the supercell band structures.

III. RESULTS

A. Supercell band structures

First, we check the convergence of key structural parameters to make sure the supercell DFT calculation is a good approximation to an isolated acceptor. We find that the displacements of the Si atoms are not very large (see Sec. III within the SM [25,27]); however, as we shall see later, they still dominate the acceptor potential. Next, we report the band structures of the various systems. Using the k-point paths and high-symmetry points shown in Figs. S3(a) and S3(b) within the SM [25], we compare the fcc primitive cell and the simple cubic supercells, which confirms that the states near the lower edge of the band gap in the supercells are derived from the neighborhood of the Γ-point in the primitive cell (shown in Sec. IV within the SM [25,27]). The band structures are shown in Fig. S3(c) within the SM [25,27].

In Fig. 2 we compare the band structures of the 216-atom-cell for pure (black) and doped (red) silicon within the simple cubic Brillouin zone of the supercell. We align
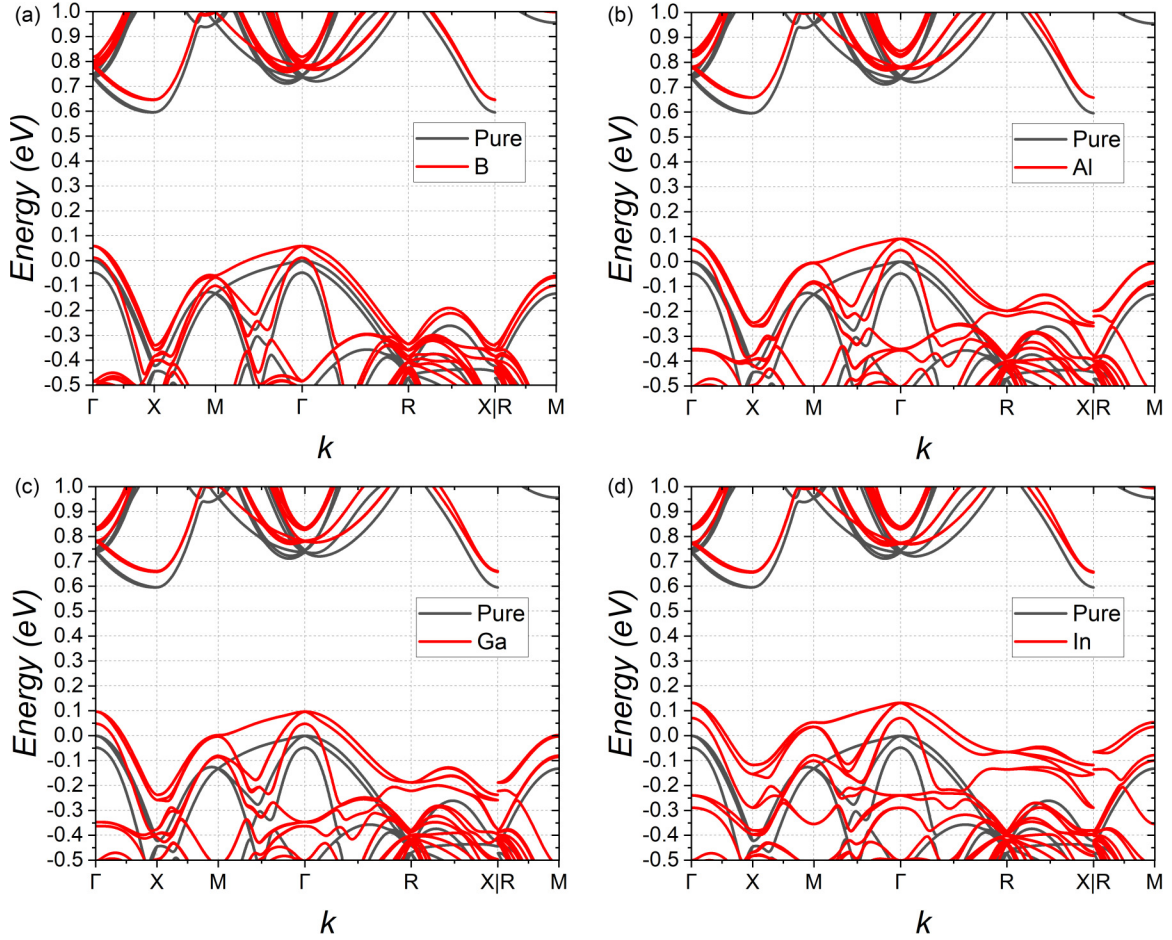
FIG. 2. Comparison of supercell band structures for different dopants {B in (a) [27], Al in (b) [27], Ga in (c) [27], and In in (d) [27]} near the Fermi energy for the 216-atom-cell pure (black) and doped (red) silicon. The k-point path within the simple cubic Brillouin zone of the supercell is shown in Fig. S3(b) within the SM [25]. The bands have been shifted to align the self-consistent potentials, as described in the text.

the self-consistent potentials as described in Sec. II D before comparing the DFT eigenvalues. The energy shifts in the high-lying valence band states caused by the dopants and the splitting of their energies resulting the spin-orbit coupling can be seen clearly. The top of the valence band lies above the Fermi energy in all the doped cases, so these systems will be metallic, as expected for periodic arrays of acceptors with densities well above the metal-insulator transition. We expect that the empty electron states lying immediately above the Fermi level will be formed largely from the overlapping bound hole states of acceptors in neighboring supercells. From Fig. 2, we can also see the dispersion of the acceptor states as a result of the interaction between acceptors, which gets smaller as the atomic number increases down Group III. The decrease of the dispersion occurs because of the greater localization of the wavefunction for the heavier elements (see Sec. IV).

We estimate the acceptor binding energies by comparing the energies to the states at the top of the valence bands at the Γ-point between pure and doped cases, after shifting as described in Sec. II D; we compare our results with those reported in previous experimental work [26] in Table II. As can be seen in Table II, the DFT binding energy estimates are somewhat larger than the experimental values; we believe this is mainly because our systems are not truly isolated dopants,

leading to two competing effects. First, the dispersion of the states tends to raise the energy of those at the Γ-point, as a result of the interaction of bound states in different unit cells, increasing the binding energy estimate. Second, the alignment of the self-consistent potentials has to be performed at a finite distance from the impurity; this means the acceptor potential is slightly lower than if the alignment were performed at infinity, decreasing the binding energy estimate. However, this second effect is small because the acceptor potential is strongly screened (see Sec. III B 2), so the first effect dominates and leads to the larger binding energy estimates in Table II. To minimize the influence from this strong screening on our central cell corrections, we will use the experimental binding energy and the screened Coulomb potential (see Sec. III B 2) during the fitting procedure described in Sec. VIII within the SM [25].

B. The impurity potential

1. The self-consistent impurity potential

We take the Al case as an example in this section. We first plot two kinds of potential differences between doped and undoped systems: in the first, we compare systems where the positions of all the silicon atoms are frozen at their relaxed

TABLE II. Estimated acceptor binding energies in DFT after aligning the potentials as described in the text, compared to previously reported experimental values [26].

Dopant	Acceptor binding energy (meV)		Shift relative to B (meV)	
	DFT	Experiment	DFT	Experiment
B	59.46	45.71	0	0
Al	91.75	70.18	32.29	24.47
Ga	97.11	74.05	37.65	28.34
In	132.3	156.9	72.82	111.2

positions in the presence of the acceptor [the "frozen lattice" case shown in Fig. 3(a)], while in the second, we compare systems where the silicon atoms are in the equilibrium positions corresponding to the doped and undoped systems [the "distorted lattice" case shown in Fig. 3(b)]. For each system we compute the total local self-consistent Kohn-Sham potential energy for the electrons (including the ionic potential, the Hartree potential and the (semi)local exchange-correlation potential) on a real-space grid and calculate the difference using the VASPKIT analysis package [28]. Note that since this is a potential energy for *electrons,* it differs by a sign change from the attractive potentials for holes discussed in Eqs. (1), (2), and (7), and is therefore positive (repulsive) near the acceptor. Also, since we use only the local potential, we do not include nonlocal contributions near the atomic cores arising from the localized PAW projectors.

In the distorted-lattice case, we observe a characteristic dipolar pattern [the yellow and blue surface around the same Si atom in Fig. 3(b)] in the potential around each Si atom. We expect that the local maximum (minimum) of the dipolar pattern will be determined by the atomic displacements; this is confirmed in Fig. S4 within the SM [25]. This is also true for the other dopant types, and will help us to predict the influence of the long-range behavior in Sec. III D.

In the frozen-lattice case this dipolar pattern is absent, as might be expected, and Fig. 3(a) shows that the largest components of the potential are more closely localized around the impurity. In particular, the tetrahedral contribution to the potential will be unphysically reduced by this approximation and the longer-range corrections to the Coulomb potential

are almost entirely removed. We will use the distorted-lattice potential difference as the basis for our calculations in the rest of the paper.

2. The effect of screening

Now we will deal with the strong screening mentioned in Sec. III A. Our aim is to estimate the potential appropriate to isolated or nearly isolated acceptors from our first-principles calculations of a relatively dense acceptor array. Since the density of acceptors in the periodic DFT calculations is above the metal-insulator transition, the resulting degenerate hole gas will screen the impurity potential. Hence, at long distances, we expect the impurity potential for holes will converge to a screened Coulomb interaction

$$V_{\text{eff,sc}}(\vec{r}) = -\frac{2}{|\vec{r}|}e^{-k_0|\vec{r}|}. \tag{7}$$

Here, k_0 is the screening wave vector that can be estimated using a linearized Thomas-Fermi model

$$k_0 = \sqrt{\frac{e^2}{\epsilon_{Si}\frac{\partial\mu}{\partial n}}}, \tag{8}$$

where $\frac{\partial n}{\partial\mu}$ is the density of states at the Fermi surface. The screening wave vector for Al is calculated in Sec. VI within the SM [25] to be $k_0 = 2.44 \, (\text{nm})^{-1} = 6.23a_0^{-1}$, using the DFT density of states in the 216-atom cell. The corresponding screening length is $k_0^{-1} = 0.41$ nm, which is smaller than the inter-acceptor spacings in the 216-atom supercell (1.64 nm), so we expect the screening effects to be strong.
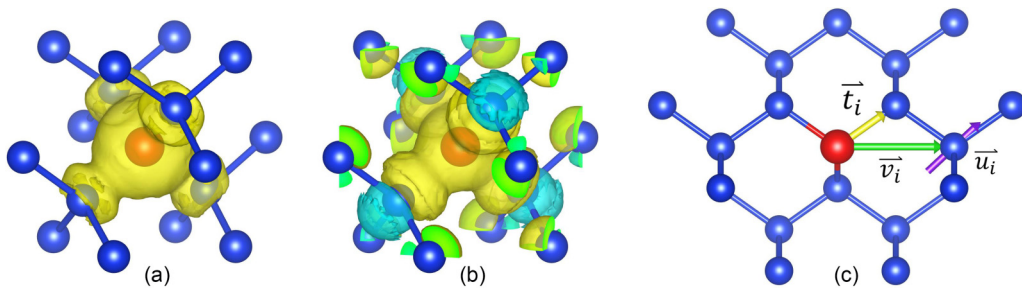

FIG. 3. (a), (b) Isosurfaces of the two potential differences used in the calculations of the Al case: (a) the frozen lattice case, and (b) the distorted lattice case. The central red ball stands for the dopant, while the blue balls are silicon atoms. The yellow surfaces are positive difference isosurfaces, while the blue surfaces are negative difference isosurfaces; the isosurfaces are truncated at a cube passing through the second-nearest neighbors, for clarity, leaving the interior of the surfaces visible (green color). (c) Samples of vectors involved in the different kinds of the central cell correction: $\vec{t}_i$ is a set of vectors connecting the acceptor to its nearest neighbors, $\vec{v}_i$ is a set of vectors pointing to next-nearest neighbors, and $\vec{u}_i$ is the unit vector in the displacement direction of atom i relative to the perfect crystal, the red ball stands for the dopant, while the blue balls are silicon atoms.
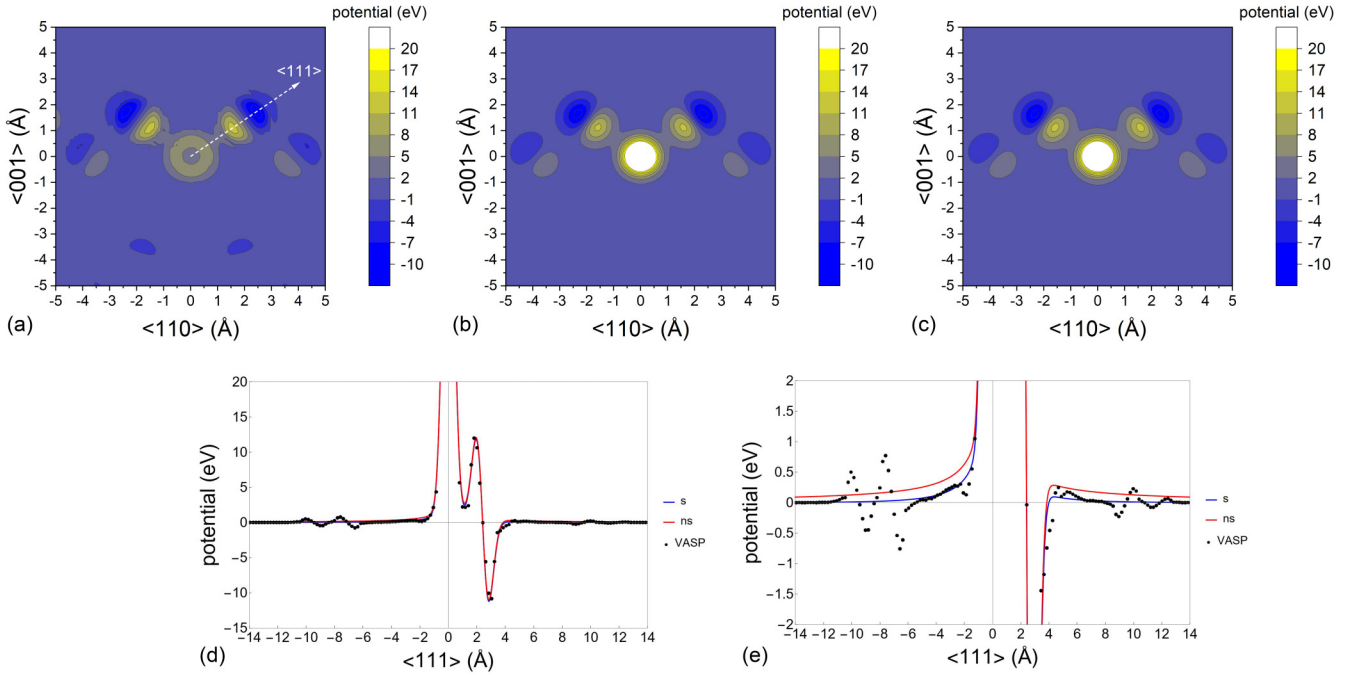
FIG. 4. The acceptor potentials of the distorted lattice in the Al case from the DFT calculation and the fitted results with next-nearest contributions. (a) Contour plot of the acceptor potential from the DFT calculation in the $(1\bar{1}0)$ plane (the $\langle 111 \rangle$ direction is shown) [27]; (b) Contour plot of the fitted potential with screening; (c) Contour plot of the fitted potential without screening; (d) Acceptor potential along the $\langle 111 \rangle$ direction through the acceptor; (e) Close-up of the central portion of the acceptor potential along the $\langle 111 \rangle$ direction through the acceptor. Here, "s" is the fit to the screened Coulomb potential, "ns" to the nonscreened Coulomb potential. The energy units for (d) and (e) are scaled atomic units. The DFT results [27] in (d) and (e) have been shifted as discussed in Sec. II D, and the points in the inner part of the Al core have been removed, as discussed in Sec. VIII within the SM [25].

C. The central cell correction

The full functional form we fit to the self-consistent DFT potential is

$$V(\vec{r}) = -V_{\text{eff,sc}}(\vec{r}) + V_{\text{cc}}(\vec{r}). \tag{9}$$

The screened potential $V_{\text{eff,sc}}$ is only used when fitting to the DFT results; once the central cell correction has been calculated, we revert to the unscreened Coulomb interaction, Eq. (2), to study its effect on the properties of an isolated acceptor. As the potential computed in the DFT calculations is for electrons while $V_{\text{eff,sc}}$ is defined for holes, an extra minus sign is required for $V_{\text{eff,sc}}$.

We then define a simple analytical form for V_{cc} and fit the parameters contained in it. As discussed below, we have investigated two choices for the distorted-lattice case, Eqs. (10) and (11), which differ in the number of neighboring Si shells included.

All fitting results shown in the figures are for the *electron* potential energy, i.e., they include the additional minus sign in Eq. (9).

The distorted lattice case directly takes the potential difference between the doped silicon and the pure silicon, and therefore includes contributions because of the atomic displacements. The potential difference has significant amplitude around the next-nearest neighbors. We therefore consider two

fits in this case: the first involves only the nearest neighbors,

$$V_{\text{cc}}^{\text{n}}(\vec{r}) = E_0 e^{-\frac{r^2}{2c_0^2}} - E_1 \sum_{i=1}^{4} (\vec{r} - b_1 \vec{t}_i) \cdot \frac{\vec{t}_i}{|\vec{t}_i|} e^{-\frac{|\vec{r} - b_1 \vec{t}_i|^2}{2c_1^2}}, \tag{10}$$

where $\vec{t}_i$ is a set of vectors connecting the acceptor to its nearest neighbors as shown in Fig. 3(c) and Sec. VII within the SM [25]. The first term has spherical symmetry, while the second term has tetrahedral symmetry and describes a symmetric contribution associated with each nearest neighbor, centered at position $b_1 \vec{t}_i$. The functional form reflects the dipolar contribution to the potential produced by each displaced atom. We use a unit vector $\frac{\vec{t}_i}{|\vec{t}_i|}$ in the definition of the nearest-neighbor term to make comparisons between different impurities more straightforward.

Our second fit for the distorted lattice case includes an additional contribution from next-nearest neighbors,

$$V_{\text{cc}}^{\text{nn}}(\vec{r}) = -E_2 \sum_{i=1}^{12} (\vec{r} - b_2 \vec{v}_i) \cdot \vec{u}_i e^{-\frac{|\vec{r} - b_2 \vec{v}_i|^2}{2c_2^2}} \tag{11}$$

where $\vec{v}_i$ is a set of vectors pointing to next-nearest neighbors, and $\vec{u}_i$ is the unit vector in the displacement direction of atom i relative to the perfect crystal. These second-neighbor sites $\{\vec{v}_i\}$ possess cubic symmetry, but the displacements $\{\vec{u}_i\}$ are almost parallel to the nearest-neighbor bonds (see Fig. 4); hence, these contributions to the potential also have tetrahedral symmetry overall. They are all shown in Fig. 3(c) and Sec. VII within the SM [25].

TABLE III. The fitting parameters for different distorted lattice cases and the R_{MAX} value from VASP database.

Parameters	B	Al	Ga	In	Donor results [19]
E_0	3.439 eV	61.38 eV	79.94 eV	116.9 eV	-1.284×10^{-3} eV
c_0	0.3401 Å	0.3731 Å	0.3481Å	0.3485 Å	1.286 Å
E_1	192.8 eV/Å	42.04 eV/Å	29.79 eV/Å	118.0 eV/Å	-2.642 eV
b_1	1.286 Å	1.384 Å	1.379 Å	1.421 Å	2.116 Å
c_1	0.4414 Å	0.4482 Å	0.4478 Å	0.4560 Å	0.9467 Å
E_2	55.14 eV/Å	15.38 eV/Å	13.01 eV/Å	28.22 eV/Å	
b_2	2.704 Å	2.739 Å	2.737 Å	2.749 Å	
c_2	0.4504 Å	0.4421 Å	0.4411 Å	0.4523 Å	
R_{MAX}	1.732 Å	1.939 Å	2.658 Å	3.168 Å	

D. Fitted parameters for Al

The fitting steps are described in Sec. VIII within the SM [25]; we constrain the fit parameters using the experimental binding energy and also exclude the region close to the defect ($r < R_{MAX}$) from the final stage of the fitting. The final results are shown in Table III along with the parameters from earlier work on donors [19]. The fit for the Al case without next-nearest-neighbor terms is shown in Sec. IX within the SM [25]. The fitted acceptor potentials are compared with the DFT calculation in Fig. 4. As shown in Figs. 4(a)–4(d), the fitted potentials both with and without screening now give good agreement with the DFT calculation in the central region around the impurity (as far as the next-nearest neighbors). Figure 4(e) shows that the screening has a significant effect on the long-range potential beyond the nearest neighbors (for $r > 4.5$ Å). The oscillations in the DFT potential for -11 Å $< r < -5$ Å and 4.5 Å $< r < 13$ Å arise from displacements in more distant neighbors that are not included in the functional forms we fit.

Most parameters are similar to those fitted without the next-nearest-neighbor terms, but the pre-factors of the spherical term E_0 and the nearest-neighbor tetrahedral part E_1 decrease slightly: including the next-nearest-neighbor terms will increase the energy, so the contributions from the other terms need to be smaller to balance this change. The parameters c_1 and c_2 representing the range of the relevant terms are small relative to the atomic spacings and approximately equal, so the contributions from the different displaced atoms are largely non-overlapping; the amplitudes E_1 and E_2 are proportional to the displacements of the atoms as shown in Sec. III B 1. The proportionality constants are calculated as 1.42×10^{-3} Å^2/eV for E_1 and 1.54×10^{-3} Å^2/eV for E_2.

Using this proportionality, we can estimate the influence of the longer-range terms that are not included in the current central cell corrections. We take the third-nearest neighbors along the ⟨110⟩ zigzag chain as example: The strength parameter E_3 is expected to be around 13.65 eV/Å according to the rule we found. As the correction of that term will also take the form like Eq. (11), the most important contribution to the potential around one of the nearest neighbors will come from the three atoms close to that point. As the effective range of the term will not change dramatically, the exponential part is about 4.6×10^{-9}. As a result, even if the displacement direction is along the vector pointing from the nearest neighbor to the third-nearest neighbor, the contribution from

the third-nearest neighbor will not beyond 5.2×10^{-7} eV ($5.3 \times 10^{-4} R_0$). Considering the current value is around 12 eV ($484 R_0$) for the top of the potential peak, the influence from the third-nearest neighbors is small enough to be ignored.

As discussed above, fitting parameters are not strongly sensitive to the inclusion of next-nearest-neighbor terms, and the influence from the third-nearest neighbors is even smaller. We use the next-nearest-neighbor fit to the central cell correction in our further discussion of the corrected wavefunctions in Sec. IV to achieve a high accuracy and get a more general picture of the influence from the corrections. Similar fits for other Group III dopants can be found in Sec. X within the SM [25].

IV. DISCUSSION

In this section, we investigate the effect of the central cell correction on the long-range electronic structure of the acceptor using envelope function models, which are believed to be reasonable approximations for a range of acceptor dopants [20–22]. We first consider the states of an isolated impurity, especially their degree of localization and their angular variation. Then we consider the implications of the changes in these states for the electronic structure of multi-acceptor clusters.

A. States of an isolated impurity

1. Probability density

We calculate the change in the wavefunction arising from the central cell correction and compare the total probability densities for the four degenerate ground states along high-symmetry directions with and without the central cell correction in Fig. 5(a). The correction produces only small changes to the probability density at the short ranges (below $1.5a_0$), with the largest effects coming from the change to the long-range decay of the state arising from the shift in binding energy. In all cases the state decays more rapidly along ⟨100⟩ than in the other directions. In order to pick out the symmetry-lowering effect of the perturbation, in Fig. 5(b) we show the fractional difference in the probability densities between the ⟨111⟩ and the ⟨$\bar{1}\bar{1}\bar{1}$⟩ directions; the ⟨111⟩ direction passes through one of the nearest neighbors while the opposite ⟨$\bar{1}\bar{1}\bar{1}$⟩ direction does not, so this difference is sensitive to the local lowering of the symmetry from cubic to tetrahedral. The largest effect of the tetrahedral structure occurs at very short range (distances below $0.5a_0$) and produces a maximum
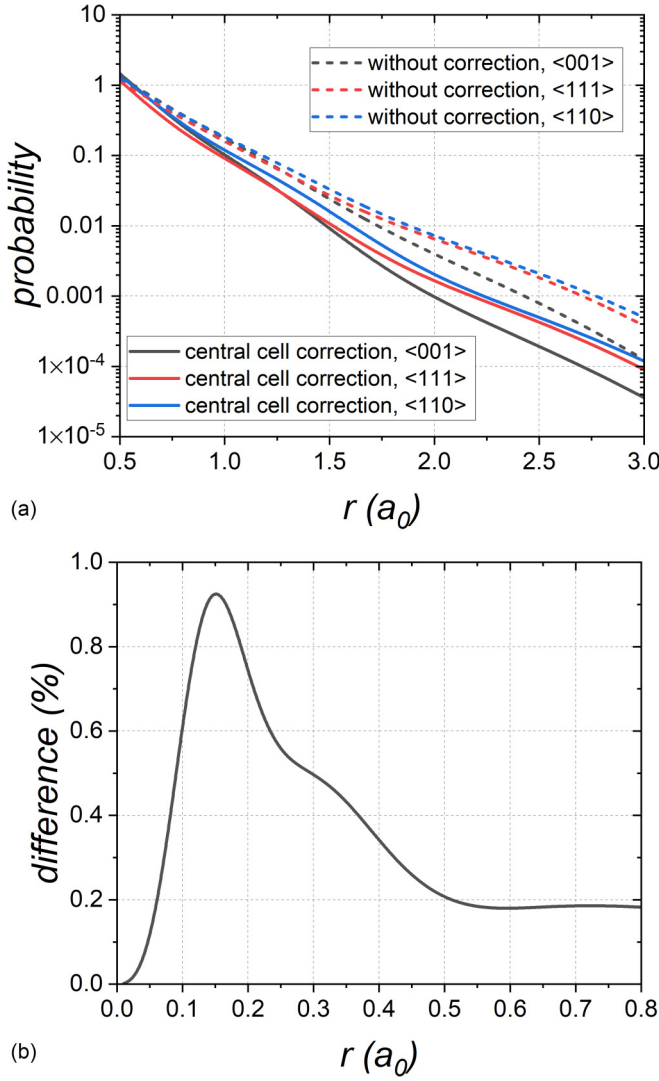
(a)

(b)

FIG. 5. Direction dependence of the total probability density for the four degenerate ground states in the Al case using the 5-Gaussian basis: (a) with (full lines) and without (dashed) the central cell correction along three high-symmetry directions; (b) percentage difference in the probability density with the central cell correction between the $\langle 111 \rangle$ and $\langle \bar{1}\bar{1}\bar{1} \rangle$ directions.

density difference between the two directions below 1%. In Sec. IV A 3, we will see the longer-range terms will make the system behave more like the cubic case and should lead to the decrease of the current value.

These results suggest the effect of the reduced symmetry of the central cell correction is localized around the nearest neighbor and does not play an important role in changing the angular nature of the states.

2. Different angular contributions to the wavefunction

Next, we look at the contributions to this direction dependence. In Figs. 6(a) and 6(b), we compare the contributions to the ground-state wavefunction (with majority contribution $m_F = +3/2$) from each angular momentum component for a pure Coulomb potential (the standard Baldareschi-Lipari model in cubic symmetry) and for our central cell
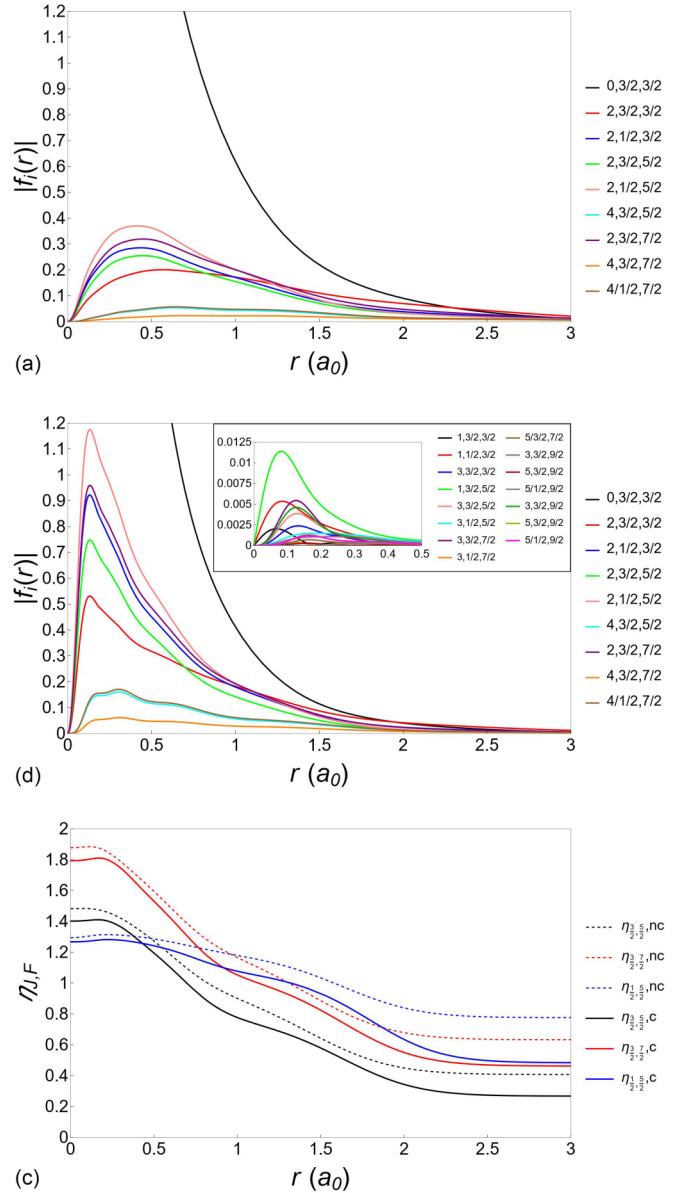

(a)

(d)

(c)

FIG. 6. Contributions to the ground-state acceptor wavefunction (in the ground state with majority contribution $m_F = +3/2$) from states of different angular symmetry in the Al case: (a) absolute value of the radial wavefunctions corresponding to different angular momentum quantum numbers $\{L, J, F\}$ in a standard Baldareschi-Lipari cubic model; (b) similar contributions to the ground state in the presence of the central cell correction. Only even-parity states are shown in the main part, while the odd-parity components are shown in the inset as they are not visible on the main scale. A 5-Gaussian expansion was used in both cases. (c) The η parameter [defined in (12)] quantifying the departure of the wavefunction from spherical symmetry as a function of distance from the acceptor. Here, "c" stands for the cases with central cell corrections, "nc" stands for no correction.

correction. The correction leads to a significantly more localized wavefunction, as we found above. Equation (6) implies that components with different angular symmetries have different behaviors at short distances (from $r = 0$ to the top of the peak): $L = 1$ components are linear at short distances,

$L = 2$ quadratic etc. The peak positions for each component are also different: components with smaller L have peaks at smaller r than those with a larger L. The components with higher L decay more slowly and at large separations ($r \geqslant 2a_0$) components with $L \neq 0$ dominate the state. The contributions from the odd-parity Γ_8^- states [the inset of Fig. 6(b)] are very small, indicating that the noncubic part of the central cell correction does not lead in itself to a large change in the symmetry of the wavefunctions.

We can parametrize the departure of the state from spherical symmetry by looking at the contributions of the dominant ($L = 2$) non-spherical contributions as a function of distance from the acceptor. For the spherical model, the ground-state wavefunction has a well-defined total angular momentum $F = \frac{3}{2}$ and therefore contains only the first three terms in Eq. (3). When the symmetry of the system is reduced (whether to cubic or tetrahedral), the ground state will include the other $L = 2$ terms with different F in Eq. (3). We examine the ratios between $L = 2$ terms with same J and different F to quantify this mixing, defined as

$$\eta_{J,F}(r) = \frac{f_{J,F}(r)}{f_{J,3/2}(r)}. \tag{12}$$

For the spherical case, these ratios are always 0 as there is no other F in the ground state. In general, $\eta_{J,F}$ will be a function of distance r from the acceptor. The results are shown in Fig. 6(c). In all cases η is greater than one at small distances but decays to a value less than one on the length scale of the scaled Bohr radius a_0, because states with higher total angular momentum ($F > 3/2$) decay more quickly than those with $F = 3/2$. The mixing ratio is slightly smaller when the central cell correction is included, because the dominant contribution from the spherical-symmetry term of the correction localizes all the states. The decay happens over a similar distance scale in both cases; with the 5-Gaussian basis used here, the ratios all tend to constants at large distances ($r \geqslant 2a_0$). However, this is a consequence of the restricted basis set described in Sec. II within the SM [25], since the radial functions in this range are all dominated by the most diffuse Gaussian ($\alpha_4 = 0.39\,a_0^{-2}$). We have checked the behavior of $\eta_{J,F}$ under the pure Coulomb potential with the richer 21-Gaussian basis described in Sec. II within the SM [25] and find $\eta_{J,F}$ behaves similarly but continues to drop out to larger distances. This suggests that the 5-Gaussian basis gives acceptable results in the distance range $r \lesssim 2a_0$ and also that the contribution with $\{L, J, F\} = \{2, 3/2, 3/2\}$ becomes the dominant one for $r > 2a_0$. For larger distances still we expect the more slowly decaying $L = 4$ states ultimately to dominate, but this regime is not well captured by our basis set.

3. Effect of the nearest-neighbor terms and longer-range terms

We estimate the energy contribution from each term in the central cell correction in the distorted lattice case by comparing separate calculations of the ground state with and without corrections and also a partially corrected case where $E_1 = E_2 = 0$. We find that the contribution from the spherical term (around $0.92R_0$ or 22.82 meV) is dominant, while the total contribution from the nearest and next-nearest neighbors is much smaller (around $0.043R_0$ or 1.06 meV for the nearest

neighbors; around $0.014R_0$ or 0.34 meV for the next-nearest neighbors). Based on the proportional relation between E_i and displacements of the atoms found in Sec. III D, we can also estimate the possible contribution from the third-nearest neighbors, which is around $0.004R_0$ (0.10 meV). It can be seen that the energy contributions from the nearest-neighbor terms and longer-range terms (such as those from the next-nearest and third-nearest neighbors) decrease approximately exponentially, which means the further terms not calculated here will have minimal contributions. It also means that the spherical term is always dominant.

This should be contrasted with the donor case [19], where the tetrahedral-symmetry nearest-neighbor term was found to be important to get a good fit to the energies of the six states of the 1s manifold and indeed dominates the fitted central cell correction as the parameter E_1 in the last column of Table III is much larger than the corresponding E_0. Although the value of E_1 in the distorted lattice is large, the positive and negative parts of the impurity potential largely cancel, given that the wavefunction varies slowly on the same length scale. This partial cancellation means the influence is much smaller than suggested by the large value of E_1.

Besides the ground-state energy, we can also estimate the contributions of longer-range terms on the symmetry of wavefunction in the same way. According to Eq. (1), the ground state under the cubic model only contains the Γ_8^+ components. The central cell corrections with tetrahedral symmetry will couple the Γ_8^+ components with Γ_8^- components, so the weight of Γ_8^- components in the normalized ground-state wavefunction reflects the significance of the tetrahedral behavior: the larger the weight of Γ_8^- components, the more significant the tetrahedral behavior. We find that the spherical term does not change the weight of Γ_8^- components as it will not reduce the symmetry, while the nearest and next-nearest-neighbor terms act to increase the weight of Γ_8^- components. We also find the next-nearest-neighbor terms play a more important role in reducing the symmetry as the increase they cause is larger. However, the estimated third-nearest-neighbor terms play an opposite role, as the weight of Γ_8^- components decreases after introducing those terms. This is because the displacements of atoms are almost parallel to the $\langle 110 \rangle$ direction from the third-nearest neighbors onwards as shown in Fig. S2(a) within the SM [25], which means the major influence of including those terms is to make the tetrahedral anisotropy [such as the difference between the $\langle 111 \rangle$ and $\langle \bar{1}\bar{1}\bar{1} \rangle$ directions shown in Fig. 5(b)] less significant.

Based on the discussions above, we suggest using the form only with the spherical term for more costly calculations, particularly for those focusing on large acceptor separations (larger than $0.5a_0$) and/or long-range behavior (such as studies of the multi-acceptor clusters mentioned later).

B. Implications for multi-acceptor structures

As we have shown previously, the single-acceptor states can be used as a basis to describe multi-acceptor structures, from pairs to chains and 2D arrays [15–17]. To investigate the effect of the central cell correction on such multi-acceptor systems, we calculate the elements of the one-hole Hamiltonian and overlap matrix elements between a pair of acceptors.
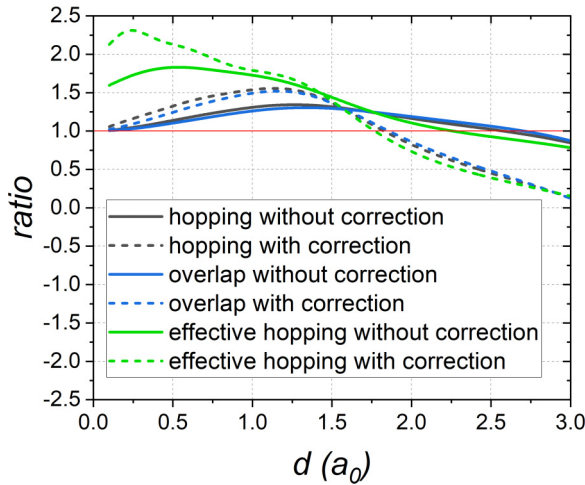
FIG. 7. The ratios between parameters of different levels for the systems with and without the central cell correction along the $\langle 001 \rangle$ direction: black lines are the results of hopping parameters, blue lines are the results of overlap parameters, green lines are the results of effective hopping parameters, and the red line stands for the case when the ratio equals to 1.

The results for separations along the $\langle 001 \rangle$ direction are shown in Sec. XI within the SM [25]; the greater localization of the states with the central cell correction significantly lowers both the overlap matrix elements (at all separations) and the hopping parameter (for separations larger than about $0.7a_0$).

To gain further understanding of the impact on multi-acceptor systems from the more localized wavefunctions, we take the two-dimensional honeycomb lattice as an example. The investigation of topological states in two-dimensional honeycomb structures goes back to the initial proposal for a topological insulator in graphene [29], which was followed by more work in analogous Group IV two-dimensional honeycomb materials including germanene and stannene [30]. Other topological effects (such as a topological magnon insulator [31]) have also been predicted in magnetically ordered honeycomb structures. Our previous work treated this system with hole basis states derived from the cubic model of a generic acceptor, Eq. (1). We identified a topological edge state in this lattice but found that the range of spacings where it occurred was dependent on the ratio of the hole-hole Coulomb interactions to the inter-acceptor hopping. In order to understand the spacings where the topological phase occurs in experiments with real acceptors, it is important to understand the effect of central cell corrections in changing the spatial extent of the states.

In the previous work [17], the driving interaction for this topological state is the difference in hopping between the $m_J = \pm 3/2$ and $m_J = \pm 1/2$ states. Therefore, we show the ratios between the hopping and overlap parameters of the $m_J = \pm 3/2$ states to those of the $m_J = \pm 1/2$ states in Fig. 7. For the convenience of further discussions, we also show the effective hopping parameters (the effective transition strengths $S^{-1/2}HS^{-1/2}$ between Löwdin-orthogonalized states, as in our previous work [15]). All these ratios cross over from above 1 to below 1 as the separation d increases and this

change happens earlier with the central cell correction, owing to the more localized wavefunctions.

In Ref. [17], the existence of the topological edge state requires the distance between two acceptors to be between $2.2a_0$ to $2.3a_0$ when one nearest-neighbor vector is aligned along the $\langle 101 \rangle$ direction. As the wavefunctions become more localized with the central cell correction, we may expect the topological edge state, like other features discussed in the previous section, to be found for smaller acceptor-acceptor distances. The upper distance limit to the predicted topological insulator (TI) phase is set by the onset of an antiferromagnetic instability driven by the on-site Coulomb interactions; these interactions increase by around 53.5% with the inclusion of the central cell corrections, mainly because of the increase in the ground-state binding energy by 52.7% and the consequently greater localization. This suggests a simple scaling approach to estimate the possible requirement for being a topological insulator with the central cell correction. The eigenvectors $\mathbf{V}_i$ satisfy the generalized eigenvalue equation

$$\mathbf{F} \cdot \mathbf{V}_i = E_i \mathbf{S} \cdot \mathbf{V}_i, \tag{13}$$

where $\mathbf{F}$ is the Fock matrix (or the single-hole Hamiltonian matrix if hole-hole interactions are neglected) and $\mathbf{S}$ is the overlap matrix. Therefore, we search for separations where the inter-acceptor elements of $\mathbf{F}$ and $\mathbf{S}$ with the central cell correction are increased by approximately 53% compared to their values at the original target separations of $2.2a_0$ to $2.3a_0$ along the $\langle 101 \rangle$ (or $\langle 110 \rangle$) direction. The new range of distances generated by this procedure is $1.5a_0$ to $1.6a_0$; similar ranges are found along other lattice directions involved in the two-dimensional honeycomb lattice calculations.

The lower-distance limit in the predicted TI is determined by the ratio of the hopping parameters for the $m_J = \pm 3/2$ and $m_J = \pm 1/2$ states. We determined these ratios both with and without central cell corrections along the directions involved in the proposed two-dimensional honeycomb lattice, using the effective hopping parameters. Comparing these ratios with and without central cell corrections, we find the corrected ratios for separations between $1.5a_0$ and $1.7a_0$ take similar values to the uncorrected ones in the original TI distance range.

Combining the results from the scaling of the upper and lower boundaries, we suggest that the TI phase is likely to occur for separations between $1.5a_0$ and $1.6a_0$; however, further calculations incorporating the central cell corrections from the outset would be required to confirm this.

C. Impact on the further investigations

In the previous sections, we have seen how the central cell corrections will influence the wavefunctions and how this will change the results from previous work on multi-acceptor systems. Now we would like to point out some more advantages of the model with central cell corrections, and the likely impact on further investigations. As mentioned in Sec. I, the cubic model is not suitable for calculations at small distances from the acceptor nucleus as the model is constructed based on the long-range Coulomb potential. By including the central cell corrections in this paper, one can introduce short-range information into the cubic envelope-function model, which

enhances the reliability of the model at the small distances while retaining the correct long-range behavior. This approach is therefore a relatively inexpensive method to check short-range behavior, which can be combined with more costly but accurate first-principles calculations to achieve higher efficiency.

Besides this improvement in describing the short-range behavior, a more significant development is that the central cell corrections introduce information about the elemental type of the acceptor into the cubic model. The cubic model includes only features that are common to all elemental types of acceptors, so it inevitably fails to describe element-specific differences. This effectively restricts the application of the cubic model to systems with a single elemental type of acceptors when the separations between them are not very small. The central cell corrections from this paper introduce information about the chemical nature of the acceptor from first-principles calculations, making it possible meaningfully to apply a cubic model to systems involving interactions between different types of acceptors.

V. CONCLUSIONS

We have shown how insight into the central-cell corrections for acceptors can be obtained from first-principles electronic structure calculations. Although the very long range of the Coulomb potential makes it impossible to access directly the limit of an isolated acceptor, we obtain short-range information about the acceptor potential from first principles in the metallic state on the high-density side of the Mott transition and combine it with an envelope-function treatment of the unscreened Coulomb potential at large distances, where the model has the cubic symmetry of the bulk crystal.

We find the largest contribution to the central-cell correction is localized on the substitutional impurity itself, while longer-range contributions are dominated by the atomic displacements along the {110} zigzag chains radiating out from the defect. We investigate the wavefunctions and the binding energy of the ground state and find, in contrast with the donor case in Si, that the overall effect of the central cell correction is mainly to increase the binding energy and correspondingly to localize the states and that this effect becomes stronger as we move down Group III; the correction will not lead to large changes in the symmetry behavior of the wavefunctions.

Our results show that the most important effect of the central cell corrections is to increase the localization of the states, implying that previous predictions arising from interactions within multi-acceptor structures will apply to smaller inter-acceptor distances than previously believed. For example, based on the new states, we estimate the range of separations for which a topological insulator is expected in a honeycomb lattice of acceptors is reduced from $(2.2 - 2.3)a_0$ to $(1.5 - 1.6)a_0$. Our short-range corrections lead to improved agreement with experiments and also allow the differing characteristics of different Group III acceptors, that all share the same long-range Coulomb potential, to be accounted for.

DATA AVAILABILITY

The data that support the findings of this article are openly available [24,26,27], embargo periods may apply.

[1] K. Sakai, *Terahertz Optoelectronics* (Springer, New York, 2005).

[2] B. E. Kane, A silicon-based nuclear spin quantum computer, Nature (London) **393**, 133 (1998).

[3] S. R. Schofield, N. J. Curson, M. Y. Simmons, F. J. Ruess, T. Hallam, L. Oberbeck, and R. G. Clark, Atomically precise placement of single dopants in Si, Phys. Rev. Lett. **91**, 136104 (2003).

[4] M. Steger, K. Saeedi, M. L. W. Thewalt, J. J. L. Morton, H. Riemann, N. V. Abrosimov, P. Becker, and H. J. Pohl, Quantum information storage for over 180 s using donor spins in a ^{28}Si "semiconductor vacuum", Science **336**, 1280 (2012).

[5] K. Saeedi, S. Simmons, J. Z. Salvail, P. Dluhy, H. Riemann, N. V. Abrosimov, P. Becker, H. J. Pohl, J. J. L. Morton, and M. L. W. Thewalt, Room-temperature quantum bit storage exceeding 39 minutes using ionized donors in silicon-28, Science **342**, 830 (2013).

[6] J. J. Pla, K. Y. Tan, J. P. Dehollain, W. H. Lim, J. J. L. Morton, F. A. Zwanenburg, D. N. Jamieson, A. S. Dzurak, and A. Morello, High-fidelity readout and control of a nuclear spin qubit in silicon, Nature (London) **496**, 334 (2013).

[7] Y. Wang, C.-Y. Chen, G. Klimeck, M. Simmons, and R. Rahman, All-electrical control of donor-bound electron spin qubits in silicon, arXiv:1703.05370.

[8] M. Kiczynski, S. K. Gorman, H. Geng, M. B. Donnelly, Y. Chung, Y. He, J. G. Keizer, and M. Y. Simmons, Engineering topological states in atom-based semiconductor quantum dots, Nature (London) **606**, 694 (2022).

[9] J. Salfi, M. Tong, S. Rogge, and D. Culcer, Quantum computing with acceptor spins in silicon, Nanotechnology **27**, 244001 (2016).

[10] J. A. Mol, R. Rahman, G. Klimeck, M. Y. Simmons, L. C. L. Hollenberg, J. Salfi, and S. Rogge, Quantum simulation of the Hubbard model with dopant atoms in silicon, Nat. Commun. **7**, 11342 (2016).

[11] M. Radue, S. Baek, A. Farzaneh, K. Dwyer, Q. Campbell, A. Baczewski, E. Bussmann, G. Wang, Y. Mo, S. Misra, and R. Butera, AlCl$_3$-dosed Si(100)-2×1: Adsorbates, chlorinated

Al chains, and incorporated Al, J. Phys. Chem. C **125**, 11336 (2021).

[12] K. Dwyer, S. Baek, A. Farzaneh, M. Dreyer, J. Williams, and R. Butera, B-doped δ-layers and nanowires from area-selective deposition of BCl_3 on Si(100), ACS Appl. Mater. Interfaces **13**, 41275 (2021).

[13] A. C. Durst, K. E. Castoria, and R. N. Bhatt, Heitler-London model for acceptor-acceptor interactions in doped semiconductors, Phys. Rev. B **96**, 155208 (2017).

[14] A. C. Durst, G. Yang-Mejia, and R. N. Bhatt, Quadrupolar interactions between acceptor pairs in *p*-doped semiconductors, Phys. Rev. B **101**, 035202 (2020).

[15] J. Zhu, W. Wu, and A. J. Fisher, Linear combination of atomic orbitals model for deterministically placed acceptor arrays in silicon, Phys. Rev. B **101**, 085303 (2020).

[16] J. Zhu, W. Wu, and A. Fisher, Multihole models for deterministically placed acceptor arrays in silicon, Phys. Rev. B **104**, 125415 (2021).

[17] J. Zhu, S. Bhattacharyya, W. Wu, and A. J. Fisher, Topological states in honeycomb arrays of implanted acceptors in semiconductors, New J. Phys. **26**, 063018 (2024).

[18] S. T. Pantelides, The electronic structure of impurities and other point defects in semiconductors, Rev. Mod. Phys. **50**, 797 (1978).

[19] J. K. Gamble, N. T. Jacobson, E. Nielsen, A. D. Baczewski, J. E. Moussa, I. Montano, and R. P. Muller, Multivalley effective mass theory simulation of donors in silicon, Phys. Rev. B **91**, 235318 (2015).

[20] A. Baldereschi and N. O. Lipari, Spherical model of shallow acceptor states in semiconductors, Phys. Rev. B **8**, 2697 (1973).

[21] A. Baldereschi and N. O. Lipari, Cubic contributions to the spherical model of shallow acceptor states, Phys. Rev. B **9**, 1525 (1974).

[22] N. Lipari and A. Baldereschi, Interpretation of acceptor spectra in semiconductors, Solid State Commun. **25**, 665 (1978).

[23] G. Kresse and J. Furthmüller, Efficiency of *ab-initio* total energy calculations for metals and semiconductors using a plane-wave basis set, Comput. Mater. Sci. **6**, 15 (1996).

[24] G. Kresse and J. Furthmüller, Efficient iterative schemes for *ab initio* total-energy calculations using a plane-wave basis set, Phys. Rev. B **54**, 11169 (1996).

[25] See Supplemental Material at http://link.aps.org/supplemental/10.1103/9k4b-q6v4 for calculating details, results for other dopants beside A1, and further discussions, which also includes Refs. [32–34].

[26] A. K. Ramdas and S. Rodriguez, Spectroscopy of the solid-state analogues of the hydrogen atom: Donors and acceptors in semiconductors, Rep. Prog. Phys. **44**, 1297 (1981).

[27] J. Zhu, J. Chen, and A. J. Fisher, DFT data supporting, figshare (online publication): 10.5522/04/28538300, 10.5522/04/28538384, 10.5522/04/28538429, 10.5522/04/28538600, 10.5522/04/28538702, 10.5522/04/28538792, 10.5522/04/28538834 (2025).

[28] V. Wang, N. Xu, J. Liu, G. Tang, and W. Geng, VASPKIT: A user-friendly interface facilitating high-throughput computing and analysis using VASP code, Comput. Phys. Commun. **267**, 108033 (2021).

[29] C. L. Kane and E. J. Mele, Quantum spin Hall effect in graphene, Phys. Rev. Lett. **95**, 226801 (2005).

[30] M. Ezawa, Monolayer topological insulators: Silicene, germanene, and stanene, J. Phys. Soc. Jpn. **84**, 121003 (2015).

[31] S. A. Owerre, A first theoretical realization of honeycomb topological magnon insulator, J. Phys.: Condens. Matter **28**, 386001 (2016).

[32] J. P. Elliott and P. G. Dawber, *Symmetry in Physics* (Macmillan, London, 1979).

[33] G. Koster, *Properties of the Thirty-Two Point Groups* (M.I.T. Press, Massachusetts, 1963).

[34] J. A. Van Vechten and J. C. Phillips, New set of tetrahedral covalent radii, Phys. Rev. B **2**, 2160 (1970).